Start-up Identification of a Pulsating Heat Pipe

Chih-Cheng Chou, Ya-Wei Lee* and Fa-Min Li

Department of Mechanical and Aerospace Engineering, Chung Cheng Institute of Technology, National Defense University

ABSTRACT

The adaptability of high-performance heat transfer devices becomes increasingly crucial along with increasing demand. Among the developed designs, pulsating heat pipes (PHP) constitute a class of adaptable cooling tools that perform much better than traditional ones. PHPs are noted to be unique for their unsteady flow oscillations that are a result of the irregular distribution of the stream of liquid slug and vapor plug. Results from experiments have shown that sensitive oscillations in start-up procedures have a significant effect on the thermal performance of PHPs.

The authors executed the present study with the objective of deriving a nonlinear autoregressive network with exogenous inputs (NARX) modeling means for investigating approaches of identifying PHP start-up procedures in the frequency domain and also in the time domain. Thus, discrete-time models were reasonably estimated and nonlinear generalized frequency response functions (GFRFs) aimed at outlining the PHP dynamics were further developed. To determine nonlinear influences exerted on PHP mass and heat transport processes under assorted operating conditions, higher-order GFRFs were broadly analyzed on the basis of observed nonlinear coupling determined to exist between assorted input spectral components.

Keywords: Start-up procedure, Dynamic diagnosis, NARX modeling, Pulsating heat pipe

脈衝熱管啟始階段識別

周志正 李亞偉* 李法憫

國防大學理工學院機械及航太工程學系

摘 要

隨著航電系統封裝規格日異提升,發展高適應性熱傳元件愈顯重要;其中,脈衝熱管兼具備高撓性與高可靠性,是現行最佳之冷卻元件。由於脈衝熱管受熱後會因為熱不穩定現象造成獨特的類規律流動振盪,不僅可以加速流體相變作用,更可因此降低高功率熱源所造成之熱負載,因此本研究目的即是利用外生輸入建模方法推導非線性自回歸網絡,利用輸入/輸出溫度因果關係建立一種可識別脈衝熱管啟動程序之離散時間模式,藉以運用於航電系統失效預判與性能診斷。

關鍵詞:啟始階段、動態診斷、非線性外生輸入建模方法、脈衝熱管

文稿收件日期 108.3.11;文稿修正後接受日期 108.5.21; *通訊作者 Manuscript received March 11, 2019; revised May 21, 2019; * Corresponding author

I.INTRODUCTION

With the intensifying diverseness of electronic device functions. miniaturization congregation of components have resulted in high power densities in the electronics industry. To meet critical requirements of thermal management, heat transfer designs with high capacity have been developed to maintain the reliability and performance of electronic products [1-3]. Among studies executed on two-phase heat transfer designs, Akachi et al. [4] proposed a promising heat pipe, called a pulsating heat pipe (PHP), which can operate without a capillary wick structure and be fabricated from a capillary metal tube bent into turns. The development of diagnosis strategies for PHPs known for featuring thermal instability could become highly promising for vaporization heat transfer devices owing to their passive thermal control. Compared with traditional capillary pumped loops as well as heat pipes, PHPs were demonstrated to exhibit more reliable gravitational field operation, higher capacity for heat transmission, and greater simplicity in terms of structure [5,6].

For analyzing the dynamic performance of PHPs, scholars have previously executed experimental explorations aimed at flow pattern visualization for ascertaining the operating mechanism of PHPs [7–9]. They have found that both sensible heat and latent heat combine to form net heat transfer in PHPs. Sensible heat dominates the overall heat transfer if the slug flow regime dominates the flow field. However, the proportion of latent heat increases as the slug flow converts to annular flow, improving the PHP performance. Changes in flow patterns elucidate the discrimination in the formation of isolated bubbles, expansion and coalescence of bubbles, slug flow, and annular flow. Compared with synchronous measurements, the oscillating features of PHPs were clarified by probing flow patterns [10]. Thus, the casualty of these measured temperature responses can be regarded as corresponding information of the operating mechanism of a PHP.

Modeling through semiempirical correlations has become the most promising approach in multiphysics coupled problems, but this approach still involves numerous limitations in practical applications. Theoretically,

practitioners have established previously statistical methods as well as empirical equations aimed at assessing two-phase flow for the purpose of forecasting heat transmission in a PHP [11-13]. Such assessments have been conceded bv researchers as merely approximations because little is known about PHP dynamics. Accordingly, for ironing out challenges emanating uncertain manufacturing processes, additional studies on this topic must still be executed. Steady-state PHP operation—occurring after PHPs have cleared start-up steps and consequently function in stable mode—has constituted the ground for constructing most black-box models [14,15]. Nevertheless, the simulation as well as the modeling of PHP initiation steps has not been adequately probed by scholars.

Because of the significance of PHP start-up steps and the influence exerted by such steps on PHP sustainability and performance, relevant scholars in this field have been stimulated to execute research on PHPs [16-18]. Start-up procedures are even marred by unanticipated events engendered by intricate PHP dynamics. Research executed for indirectly or directly probing PHP start-up modeling is limited, as ascertained by the author's literature review. In fact, the start-up scenarios depend on the vapor/liquid condition in the heating section [19]. Although start-ups under different conditions involve different liquid superheating levels in the heating section, temperature overshoot extents, and start-up times, they should not steady-state ultimately affect operations. Actually, some start-ups were reported to lead to relatively high steady-state temperatures, with some even failing to start the circulation process [20,21]. Accordingly, the two-phase dynamics inherent in the heating section exert considerable influences on the unanticipated heat seepage traveling to the cooling section.

Analyzing black nonlinear systems is crucial, although relevant research executed previously has typically described nonlinear systems by applying linear approaches; this unfavorable practice is attributable to intricacy of estimation procedures [22-24]., Practitioners have developed corresponding theories and administered them to an extensive category of systems the nonlinear on basis of Volterra-Wiener functional series

representations [25]. Volterra and Wiener's research work has constituted the footing for considerable explorations executed on the efficacious estimation of physical system kernels. Gain expansion/compression, desensitization, plus cross modulation—all created within frequencies—could occur in tandem in reality, engendering nonlinear occurrences in the frequency domain [26,27]. A prerequisite to probing nonlinear systems is a scheme for outlining such systems' dynamic performance by employing input—output (I/O) measurements, and this has been the objective of nonlinear modeling.

For the purpose of simulating as well as modeling chaotic systems, relevant practitioners in the field have extensively implemented artificial neural networks (ANNs)-known to be data-driven models and to constitute vital approaches for modeling black-box systems—with machine learning techniques [28,29]. ANNs find primary application in revealing the relationships between system variables through the employment of gauged system performance data or model (based on physics)-derived data. Thus, ANNs have been regarded as good alternatives to conventional approaches for system diagnosis. A typical ANN comprises several simple and interconnected processing units. The units' layers are organized to ensure that data inputted at the input layer reaches the output layer after traversing through a single or through several intermediate layers. ANNs provide an option to address complex and ill-defined problems and are used in many engineering applications, because they offer reasonable solutions. This more study ANN-based established an nonlinear autoregressive network with exogenous inputs (NARX) modeling means suitable for nonlinear system diagnosis in the discrete-time domain [30-32]. Generalized frequency response functions (GFRFs) derived from the NARX models could be used to illustrate the PHP dynamics from the viewpoint of energy.

II. EXPERIMENTAL

The experimental setup in the executed study comprised a power supply unit, designed PHP, and high-speed data acquisition system (Fig. 1). The geometric configuration of this PHP was

symmetrical, and a copper capillary tube constituted the entirety of the pipe; the tube's measured wall thickness and inner diameter were determined to be 1 and 3 mm, respectively. Furthermore, the PHP dimensions were 135 mm \times 135 mm \times 320 mm, and an 8-mm bending radius was measured for the 16 U-turns made in either end. A 70-mm heating section was covered and the rest of tube as the cooling section was exposed to the environment. An electrical power supply unit (GITEK Electronics, model GR-11H12H, Taiwan) was used to apply a heat source through a Ni-Cr coil (Omega Engineering, model NIC80, USA) wrapped around the heating section at equivalent 3-mm intervals. A three-way valve mounted on the PHP was employed to facilitate vacuuming and filling the PHP with working medium using a syringe. The vacuum of the PHP was kept at 10-2 Torr before the working medium was filled. Deionized (DI) water was chosen for the working medium for safety considerations and its high merit number relative to other cooling media. A medium filling ratio of 50% was chosen, and the net DI water loaded into the weighed using an electronic was microbalance (Shinko Electric Industries, model HT-220E, Japan), with minimal uncertainty of ± 0.01 g.

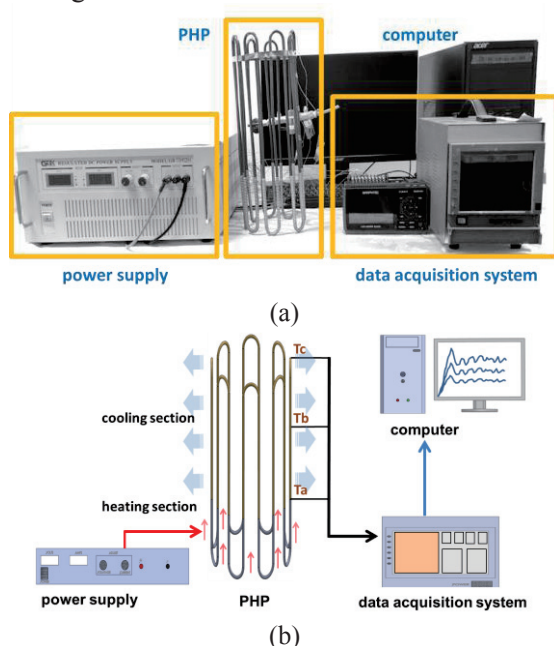


Fig. 1. (a) Photo and (b) schematic of the established setup of the designed PHP system employed for thermal analysis.

The PHP was tested in vertical bottom heating

mode without any auxiliary cooling design. A range of stable voltage output (2-220 V) was acquired by regulating the electrical power supply unit. An unchanging heat flux boundary condition relevant to the heating section was engendered by the established heating setup in this study; 40, 80, and 120 W served as the heating powers for the test. After the heat was absorbed by the heating section, it was directly transferred throughout the cooling section through conduction via the solid tube and convection via the working medium and finally released to the environment. A total of three calibrated T-type thermocouple wires connected to the data acquisition system (Graphtec Corporation, model GL240, Japan) at equivalent 75-mm intervals were employed. The locations of each of the mentioned thermocouples were distributed along the cooling section: that is, Ta, Tb, and Tc. Every experiment was conducted for exactly 10 min, and all the temperature data were sampled at a time interval of 0.2 s under a $26^{\circ}\text{C} \pm 1^{\circ}\text{C}$ environment. The PHP performance was evaluated in terms of the entire thermal resistance, represented by

$$R = \left(\overline{Ta} - \left(\overline{Tb} + \overline{Tc}\right) / 2\right) / Q_{in}, \qquad (1)$$

where Qin is the heat input and the overline represents mean value.

Ⅲ. MODELING STRATEGY

Modeling the effect exerted on nonlinear stochastic dynamical systems has been of interest for academia. Through the execution of nonlinear regression with an ANN, massive historical time series can be trained, and such a nonlinear system can then be represented as a discrete-time NARX model. The introduced ANN based on radial basis functions (RBFs) [33-35] was noted to be constituted by a hidden layer involving j neurons, an input layer involving m nodes (corresponding vector form denotation: $u(t) = [u_1(t), \dots, u_m(t)]$), and an output layer involving n nodes (corresponding vector denotation: $y(t) = [y_1(t), \cdots, y_n(t)]$. All mentioned input nodes are connected by using the same unity weight to all hidden layer neurons. By contrast, all mentioned nodes constituting the hidden layer are connected by using different weights to the output nodes (Fig.

2). In this ANN structure, by typically executing a Gaussian-type function [36,37], each neuron determines the span from its center to the input; via nonlinearity, the neuron subsequently transmits the derived scalar. The nth hidden neuron's output is typically presented as follows: $\Phi(\|U(t) - cj\|)$, (2)

with Φ (•) and cj representing the nonlinear basis function and the center of the hidden layer's jth node, respectively.

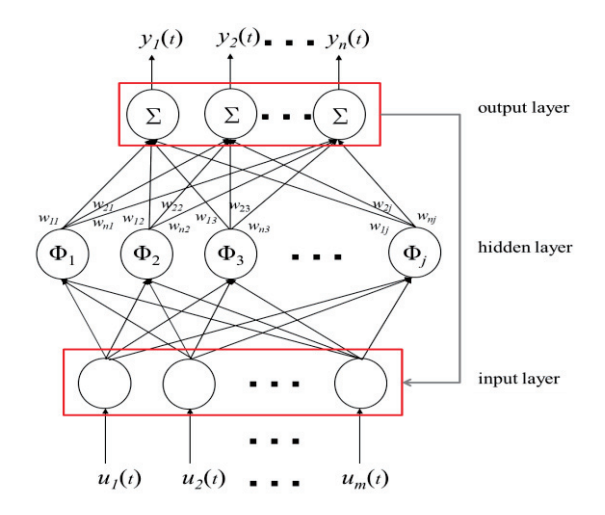


Fig. 2. Nonlinear multiple-input and multiple-output functional ANN structure.

A NARX model with a single input–single output feature is typically presented as follows:

$$y(t) = \alpha + F^{t}[y(t-1), \cdots, y(t-n_{y}), u(t-d), \cdots, u(t-d-n_{u})]$$
(3)

Here, d, n_u , n_y , and ℓ represent the time delay for the system, maximum lag for input, maximum time lag for output, and nonlinearity degree, respectively. In addition, y(t), α , u(t), and $F[\, \cdot \,]$ denote the system output, constant vector term aimed at accounting for mean levels, system input, and nonlinear function that is vector valued, respectively.

A critical task in modeling is the derivation of a NARX model that can yield a nonlinear system's representation parsimoniously. Moreover, the structure of such a derived model ought to be adequate; this is because achieving this requirement ensures that the entirety of the dynamics can be adequately detailed and that overfitting and numerical problems are evaded. An orthogonal estimator constitutes a noncomplex as well as efficacious method enabling the estimation of each individual model

coefficient. Each individual model term's contribution to the output of a system can be manifested using the error reduction ratio (ERR) [38,39], which is typically presented as follows:

$$ERR_{i} = \frac{\sum_{\tau=1}^{N} g_{i}^{2} w_{i}^{2}(\tau)}{\sum_{\tau=1}^{N} y^{2}(\tau) - \frac{1}{N} \left[\sum_{\tau=1}^{N} y(\tau)\right]^{2}} \times 100\%$$

where N, g_i , and w_i denoting the number of implemented observations, coefficients, and auxiliary model terms, respectively. Such an auxiliary model is established in a manner that ensures the orthogonality of the w_i terms to the data records.

The term demonstrating the largest ERR (i.e., the term identified as having the largest contribution to residual variance reduction) is identified via a forward-regression algorithm at each step. An information criterion serves as the trigger applied to halt the procedure. The Akaike information criterion (AIC) [40,41] exemplifies such a criterion, which is typically presented as follows:

$$AIC = N \log_{e} \left(\sigma_{\varepsilon}^{2}\right) + kp , \qquad (5)$$

where k and σ_{ε}^{2} representing a factor of penalty and the variance of p-term-model-related residuals, respectively. The derived model forestalls solution trapping in local minima—a common in ANN-based models—because it is inherently nonlinear with regard to its variables but is linear with regard to its parameters. Residuals obtained for a nonlinear system is unpredictable when using all nonlinear and linear combinations of previous outputs and inputs. However, through model validation testing, expressed as follows, the convergence of the residuals in the learning process can be determined:

$$\phi_{\varepsilon\varepsilon}(\tau) = \delta(\tau), \tau \neq 0, \tag{6}$$

$$\phi_{u,\varepsilon}(\tau) = 0 , \forall \tau, \qquad (7)$$

$$\phi_{(u_i u_j)' \varepsilon}(\tau) = 0 , \forall \tau , \qquad (8)$$

$$\phi_{(u,u_{\tau})^{*}\varepsilon^{2}}(\tau)=0,\forall \tau, \qquad (9)$$

$$\phi_{\varepsilon^{\frac{2}{u}}}(\tau) = 0 , \forall \tau \ge 0, \qquad (10)$$

where a 95% confidence interval being assumed in these residual validations and $\phi_{ab}(\tau) = E[a(t-\tau)b(t)]$. In addition, $u(\tau)$, $\delta(\tau)$, the prime

symbol, and $\varepsilon(\tau)$ in the foregoing equations denote the input sequence, Kronecker delta [42,43], mean removal (i.e., mean has been omitted), and residue sequence, respectively.

This modeling strategy was based on experimental data, including the effect of noise. By contrasting real and model outputs, this study derived the deviation of the model using the RMSD [44,45]—which estimates the deviation of model-forecast values from real values obtained in the modeled environment—and square value of Bravais—Pearson correlation coefficient (R^2) [46]. The individual deviations estimated in the RMSD are actually residuals and are combined in the estimation process to realize one measure of predictive power. Here, the normalized RMSD (NRMSD) served as one of criteria employed to evaluate model accuracy, and its expression form is detailed subsequently:

$$RMSE = \sqrt{\frac{\sum_{i=1}^{N} (o_i - y_i)^2}{N}},$$

$$NRMSD = \frac{RMSD}{o_{\text{max}} - o_{\text{min}}},$$
(11)

where y_i is the i^{th} simulated value corresponding to o_i and o_i the i^{th} observed value.

 R^2 is a suitable measure of association when couples of continuous data follow a bivariate normal distribution. When there is a complete association, two straight lines overlap with a positive slope (i.e., $R^2 = 1$), signifying a perfect simulated result without deviation. R^2 is another criterion to confirm the accuracy of models; its expression form is

$$R^{2} = \frac{\sum_{i=1}^{N} (y_{i} - \overline{y}) (o_{i} - \overline{o})}{\sqrt{\sum_{i=1}^{N} (y_{i} - \overline{y})^{2}} \sqrt{\sum_{i=1}^{N} (o_{i} - \overline{o})^{2}}}, \quad (12)$$

where o and y are mean values of observed and simulated results, respectively.

For linear systems, spectral analysis is an entrenched and extensively executed process in engineering. Traditionally, spectral densities and frequency response functions have been estimated using the fast Fourier transform algorithm and window functions. However, most systems in actual-world problems are, to some

extent, nonlinear, and unfortunately, applying linear spectral estimation procedures to data generated from nonlinear systems can introduce significant errors. A qualified NARX model mapped into the frequency domain and can precisely illustrate a system's nonlinear as well as linear features. From the vantage point of energy transfer, GFRFs are used for PHP dynamics diagnosis. By definition, GFRFs constitute products of multidimensional Fourier transforms of kernels [47,48] and are derived using a Volterra series:

$$y(t) = \sum_{l=1}^{\infty} y_{l}(t) , \qquad (13)$$

where the $y_{i}(t)$ is the n^{th} -order output typically being

$$y_{l}(t) = \int_{-\infty}^{\infty} \cdots \int_{-\infty}^{\infty} h_{l}(\tau_{1}, \cdots, \tau_{l}) \prod_{i=1}^{l} u(t - \tau_{l}) d\tau_{l}, n > 0, (14)$$

where τ and $h_i(\tau_1, \dots, \tau_i)$ are known to constitute system time lag and lth-order impulse response, respectively. An lth-order GFRF can be derived by directly administering a multidimensional Fourier transform to $h_i(\tau_1, \dots, \tau_i)$. The definition of the mentioned function is

$$H_{l}(f_{1}, \cdots, f_{l}) = \int_{-\infty}^{\infty} \cdots \int_{-\infty}^{\infty} h_{l}(\tau_{1}, \cdots, \tau_{l}) e^{-j2\pi(f_{1}\tau_{1} + \cdots + f_{l}\tau_{l})} d\tau_{1}, \cdots, d\tau_{l}$$

$$\tag{15}$$

Subjecting Eq. (15) to an inverse transform subsequently yields its corresponding nonlinear lth-order impulse response:

$$h_{i}\left(\tau_{1},\cdots,\tau_{i}\right)=\frac{1}{\left(2\pi\right)^{n}}\int_{-\infty}^{\infty}\cdots\int_{-\infty}^{\infty}H_{i}\left(f_{1},\cdots,f_{i}\right)e^{j2\pi\left(f_{i}\tau_{1}+\cdots+f_{i}\tau_{i}\right)}df_{1},\cdots,df_{i}$$

The system's lth-order output can be derived by substituting Eq. (16) into Eq. (14) and performing several processes of integration on τ_1, \dots, τ_r :

$$y_{i}(t) = \frac{1}{(2\pi)^{s}} \int_{-s}^{s} \cdots \int_{-s}^{s} H_{i}(f_{i}, \cdots, f_{i}) \prod_{i=1}^{l} U(f_{i}) e^{i2\pi f_{i}} df_{i}, \qquad (17)$$

where the input spectrum is represented by $U(f_i)$. The well-known form of the foregoing equation in the frequency domain can now be derived by executing the multidimensional Fourier transform on either side of Eq. (17):

$$Y_{t}(f_{1}, \cdots, f_{t}) = H_{t}(f_{1}, \cdots, f_{t}) \prod_{i=1}^{t} U(f_{i}), \qquad (18)$$

Thus, for a typical l^{th} -order subsystem that is homogeneous, $H_{\tau}(f_1, \dots, f_t)$ and $h_{\tau}(\tau_1, \dots, \tau_t)$ are, respectively, frequency- and time-domain representations of equivalent transfer functions that are not reliant on the input excitation. For GFRF computation, u(t) is postulated as being the total value of K sinusoids

$$u(t) = \sum_{k=1}^{K} a_k e^{j2\pi f_k t}, \qquad (19)$$

where a_k denotes the amplitude. The lth-order output could be acquired by substituting Eq. (19) into Eq. (14):

$$y_{l}(t) = \int_{-\infty}^{\infty} \cdots \int_{-\infty}^{\infty} h_{l}(\tau_{1}, \cdots, \tau_{l}) \prod_{i=1}^{l} \sum_{k=1}^{K} a_{k} e^{j2\pi f_{k}(t-\tau_{i})} d\tau_{i},$$

$$= \sum_{k=1}^{K} \cdots \sum_{k_{i}=1}^{K} \prod_{i=1}^{l} a_{k} e^{j2\pi f_{k}(t-\tau_{i})} \int_{-\infty}^{\infty} \cdots \int_{-\infty}^{\infty} h_{l}(\tau_{1}, \cdots, \tau_{l}) \prod_{i=1}^{l} a_{k} e^{j2\pi f_{k}(t-\tau_{i})} d\tau_{i}$$
(20)

Inputting Eq. (15) into Eq. (20) yields the following:

$$y_{l}(t) = \sum_{k=1}^{K} \cdots \sum_{k_{l}=1}^{K} \left[a_{k_{1}}, \cdots a_{k_{l}} H_{l}(f_{k_{1}}, \cdots, f_{k_{l}}) \right] e^{-j2\pi \left(f_{k_{1}} + \cdots + f_{k_{l}}\right)t}$$
(21)

The Fourier transform executed for Eq. (21) becomes an aggregation of delta functions when $a_k = 1$ (corresponding to the entirety of k = 1, 2, ..., 1) and K = 1:

$$y_{l}(t) = \sum_{k=1}^{l} \cdots \sum_{k_{j}=1}^{l} H_{l}(f_{k_{1}}, \cdots, f_{k_{l}}) e^{-j2\pi(f_{k_{1}} + \cdots + f_{k_{l}})t}, (22)$$

The invariance property of GFRFs to system input is highly desirable, because it enables the characterization of nonlinear systems without a priori knowledge of inputs. Thus, the advantage of GFRFs can be utilized to reveal the PHP dynamics by capturing the sensitive spectral effects engendered by parameter variations, thus providing valuable insights into system behavior.

IV. RESULT AND DISCUSSION

The proposed PHP was determined to manifest features of unstable motion, which are similar to those of Lorenz chaos [49,50]. Heating applied to the bottom of the heating section causes uneven pressure among the parallel tubes and then induces fluid oscillations, forming the operating mechanism of PHPs. These self-maintained flow oscillations

influence the liquid film thickness determined for the vapor and liquid phases of the working medium on the internal surface. This drop in thickness determined for the liquid film can be regarded as a switch for the transition of flow patterns, resulting in intermittent flow dynamics.

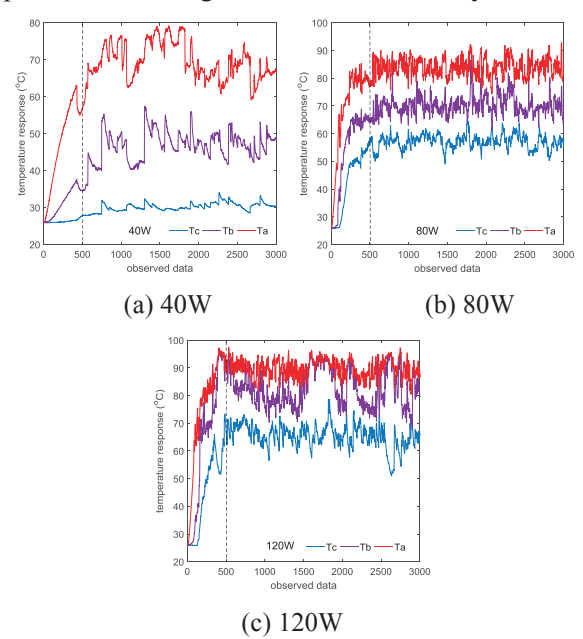


Fig. 3. Temperature variations derived for Ta, Tb, and Tc.

Fig. 3 shows the temperature responses determined for Ta, Tb, and Tc at low, medium, and high heating powers of 40, 80, and 120 W. At initial operation, nuclear pool boiling could be recognized to be a main heat transfer mechanism of the PHP due to the stable enhancement of the observed temperatures. Since consistent flow oscillations occurred, latent heat dominated the transfer mechanism. During normal operation, the temperature variations indicated that flow pattern in the PHP changed transiently and repeatedly due to the thermal equilibrium of the PHP. At 40 W, the noted slug flow was determined to oscillate with obvious temperature variations at 85 s (Fig. 3(a)). However, a tiny increment was found in Tc before 120 s, showing the PHP was unable to operate entirely until the aggregated heat energy was large enough to vaporize the working medium to drive the flow. When the set heating power surpassed 80 W, the flow oscillated much faster, representing vapor plug disintegration into more fragments. On account of the foregoing experimental results, one can conclude that the effect of thermal instability

was enhanced with heating powers (Fig. 3(c)-(c)). Such assorted thermohydrodynamics engender vapor plugs and liquid slugs unevenly distributed over the entirety of a system; just some tiny thermal instability can engender frequent changes in the plug and slug flow directions. As determined from the last 1500 observed data, the entire thermal resistances of the PHP derived via Eq. (1) were 0.74, 0.26, and 0.14 °C/W for the three foregoing heating powers. This validates this PHP to be suitable for managing an extensive range of heat sources.

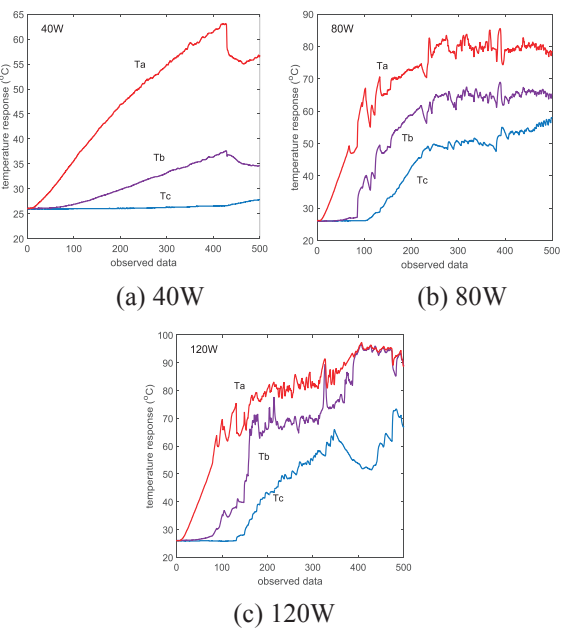


Fig. 4. Temperature variations derived for Ta, Tb, and Tc during initial operation of PHP.

The study selected the initial 100 s of each measurement, including the duration from stagnation to quasi-steady state, for modeling the casualty of temperatures in the PHP start-up (Fig. 4). Temperatures increased steadily at the low heating power of 40 W (Fig. 4(a)), showing that temperature hysteresis occurred and that this start-up procedure was mainly dominated by thermal conduction. Due to low heat input and gravity effects blocking the flow oscillation, the tube flow was maintained in liquid phase. When the heating level was set to surpass 80 W, sensitive temperature variations, but without overshoots, were noted in the start-up procedure (Fig. 4(c)–(c)). This informed that an adequate heating power for vapor influx realization can not only enable gravity resistance but also pump liquid slug. The phase transition of the applied working medium became more severe than before because the vapor plugs broke into fragments and the flow speed increased. With the enhancement of convection effects, more dramatic oscillations occurred and overcame the surface tension; the corresponding flood could change the shape of the vapor—liquid interface. This changed the pressure distribution and therefore the fluid movement direction.

As noted above, during the operation of the PHP, flow convective boiling and nucleate boiling could intensify two-phase interactions, leading to complicated flow movements with a sporadic distribution of vapor plugs and liquid slugs. To understand the PHP dynamics in start-up procedures, an efficacious NARX model was established. Because order selection and time delay settings were noted to be important to the nonlinearity of the model structure, this study set the utmost time lag for output as well as input to 20 through trial and error. In addition, the most 15 important terms were selected, and other candidate terms were discarded by defining the threshold value of the ERRs. Because the ERR computation and parameter estimation were conducted concurrently to identify the importance of each individual NARX model term, the structure terms were all ordered depending on their measured input to the global mean squared prediction error. The models listed in Table 1 through 3 represent the cause-effect relations of Ta(t)-Tb(t) as well as Tb(t)–Tc(t), for the heat transfer process through the lower and upper halves of the cooling section. These diagnostic models, named as Tb(t) and Tc(t), consisting of historical temperature time series were noted to exhibit a common feature of self-prediction involving forecasting of the most important term one step in advance before the output value. Some cubic terms were assessed in the model Tc(t), implying that more intensive conjugate heat transfer existed in the upper cooling section as the heating power increased. The model validation tests executed in this study revealed all models to be reasonable (Fig. 5); this is due to the fact that the convergence degrees determined for 50 lagged residuals for Eqs. (6)–(10) were almost within the defined 95% confidence interval. To demonstrate the models' capacity to simulate physical PHP behavior during start-up procedures, the simulation-derived results were compared against the measured results (Fig. 6).

With the exception of some tiny deviations, over 97% of the simulation-derived results were determined to be within a relative error of less than $\pm 30\%$ (Fig. 7). The satisfactory agreement levels were also confirmed by NRMSD and R2, with the NRMSD values being estimated to be within a tiny range of 0.01825-0.06695 and R2 values being noted to be within the range of 0.96870-0.99954 and to follow a positive slope. Thus, the black-box method executed in this study for transient assessment has promise for use in procedures aimed at deriving diagnostic data for PHPs. Further research work can be performed on the capacity of the applied NARX model to execute forecasts multiple steps in advance for optimizing PHP design.

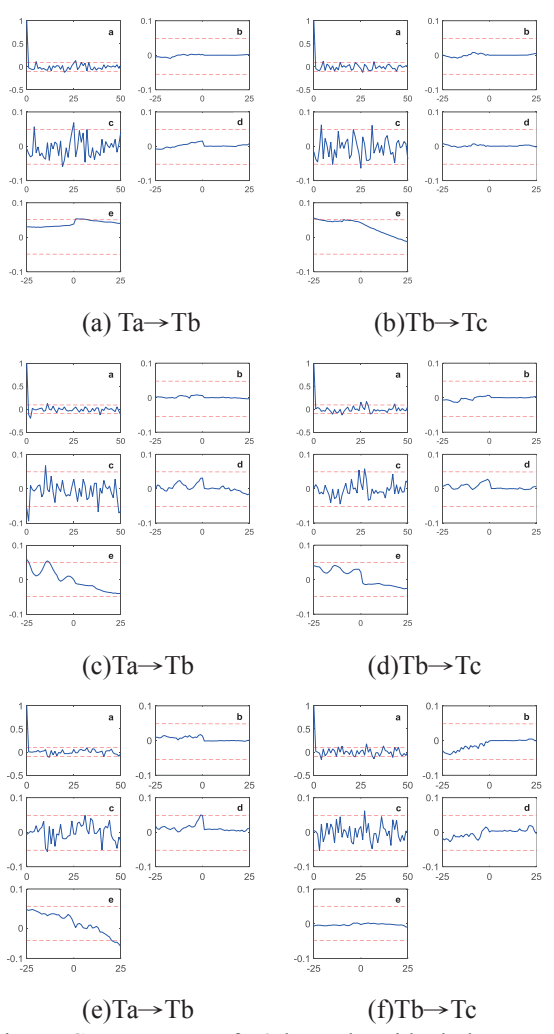


Fig. 5. Convergence of 50 lagged residuals by means of model validation tests, where (a) and (b) are for 40 W, (c) and (d) are for 80 W, and (e) and (f) are for 120 W. (tests a \sim e are followed as Eq. (6) \sim (10))

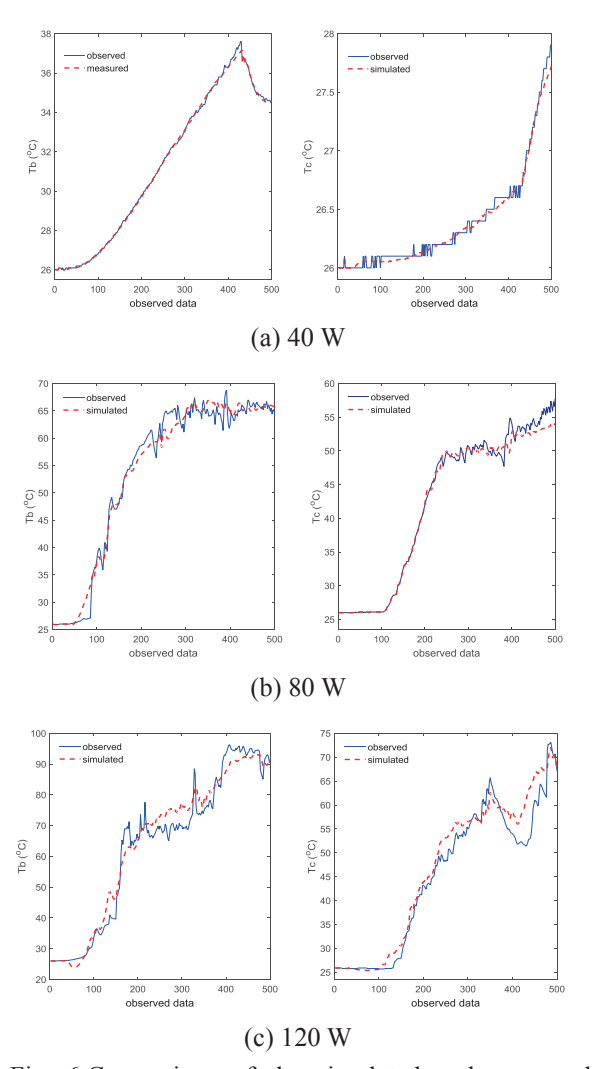
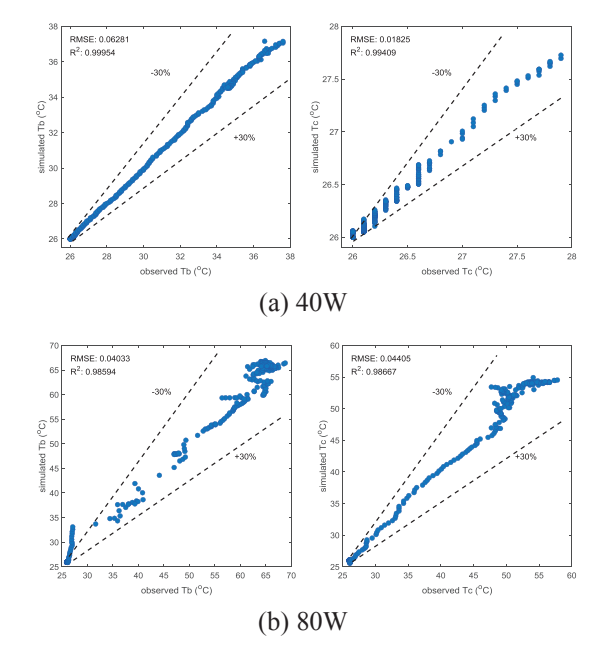


Fig. 6.Comparison of the simulated and measured Tb(t) and Tc(t).



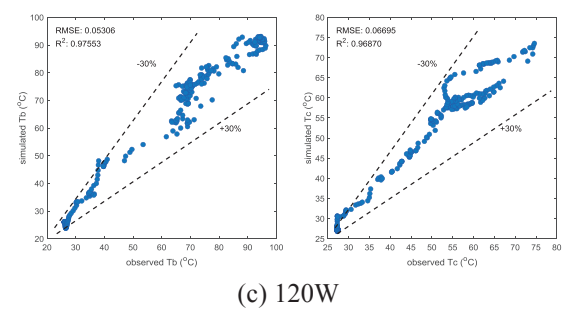
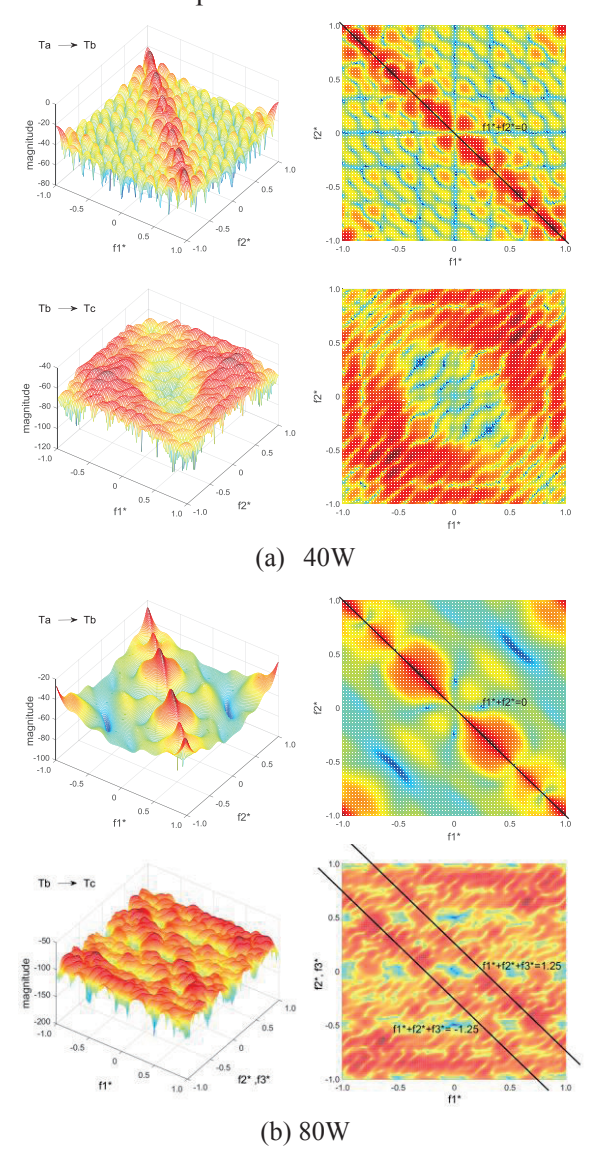


Fig. 7. Correlation determined between observed and simulated Tb(t) and Tc(t).

When discrete-time NARX models are being subjected to mapping in the frequency domain, the energy spectra representing PHP dynamics can be revealed by GFRFs. First-order GFRFs are just single-frequency spectra without nonlinear effects. Although multiperiodic features can be ideally found, these linear features cannot fully describe the operating mechanism of a chaotic PHP, such as that designed in the current study. To recognize the nonlinearity of PHP dynamics, the highest GFRF for each model was proposed to be analyzed (Fig. 8). These nonlinear effects were emphasized as resonances on the responding surfaces, which suggested the PHP possessed nonlinear dynamics around these frequency features. These resonances became ridges and antiresonances became valleys, allowing for further understanding of the energy aggregation and expansion during the PHP start-up procedure. The negative frequency axis depicted in Fig. 8 is theoretically a mirror image of the positive frequency axis. Here, the sampling rate of each measurement was 5.0 Hz, and multiplying this rate by the resonance frequency that was normalized could yield the distinct actual values. Ouite different from observations noted for the first-order GFRFs, the output energy at these frequency ranges was produced by the heat transfer mechanism of the PHP, causing a strong intermodulation between the frequencies. There were many cross ridges, but the main ridges dominated the nonlinear effects on energy transition. At 40 W, only a distinct resonance peak at 0 Hz was recognized in the lower cooling region. However, a deduction in this paper is that heat could not efficiently transfer to the upper section due to the antiresonance spectrum (Fig. 8(a)). At 80 W, energy aggregations at nearly ±5.75 Hz gradually formed in the upper section, signifying that more heat was transferred to the top through a regular mode of transfer (Fig. 8(a)). When the heating power was scaled up to 120 W, dense spectra of narrow resonances appeared, with the spectra being recognized at 0 and ± 5 Hz in the lower section and at 0 and ± 10 Hz in the upper section (Fig. 8(c)). Compared with the obtained resistances, thermal such a statistically demonstrated coherence in resonance noted in the start-up procedure could engender a favorable PHP performance.



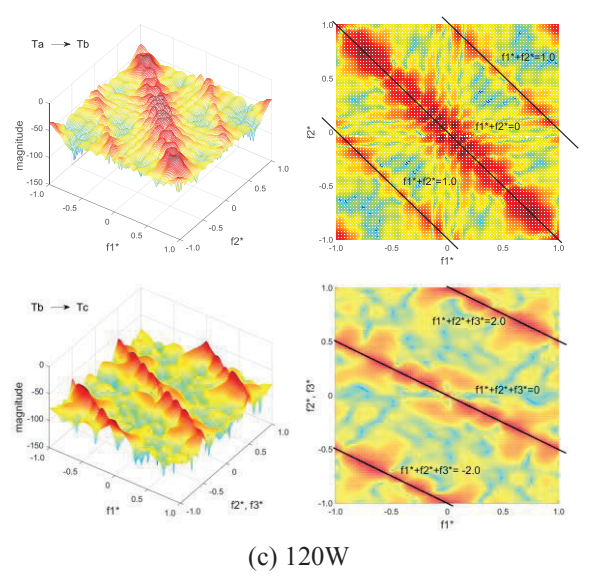


Fig. 8. Resonance spectra for heat transfer in lower and upper cooling sections.

Table 1. NARX models for diagnosing PHP dynamics at 40 W.

at 40	at 40 W.				
model	terms	coefficient	ERR	Standard deviation	
	Tb(t-1)	+8.18400E-01	9.99990E-01	0.11405	
	Ta(t-2)Ta(t-3)	+2.08840E-03	1.54460E-06	0.00113	
	Tb(t-3)Tb(t-3)	+3.60740E-03	4.80120E-07	0.00109	
		+3.71330E+00	4.66460E-07	0.07430	
	Ta(t-1)Ta(t-8)	-8.50310E-03	3.39860E-07	0.00470	
	Ta(t-1)Ta(t-3)	-4.56110E-03	1.70770E-07	0.00177	
	Ta(t-14)Ta(t-14)	-6.02890E-03	9.13010E-08	0.00254	
Tb(t)	Ta(t-1)Ta(t-5)	+4.13180E-04	8.85700E-08	0.00026	
- (-)	Ta(t-2)Ta(t-2)	-4.33760E-03	6.40780E-08	0.00298	
	Ta(t-8)Ta(t-14)	+8.11130E-03	6.26700E-08	0.00428	
	Ta(t-1)Ta(t-1)	+4.03180E-03	5.98890E-08	0.00283	
	Ta(t-2)Ta(t-14)	+6.63880E-03	4.89780E-08	0.00552	
	Ta(t-1) Ta(t-13)	+8.89980E-02	3.90000E-08	0.14646	
	Ta(t-15)	-4.09700E-04	3.17170E-08	0.00022	
	Ta(t-14)	-7.21120E-02	2.07850E-08	0.13290	
	Tc(t-1)	-1.99410E+00	9.99210E-01	0.46170	
	Tc(t-2)	-4.34360E+00	4.83320E-04	0.37251	
	Tc(t-3)Tc(t-3)	+2.89210E-02	5.84630E-05	0.07322	
	Tc(t-3)	-1.38090E+00	4.33180E-05	0.19614	
	Tc(t-1)Tc(t-1)	+7.60550E-01	1.97600E-05	0.52082	
	Tb(t-14)Tb(t-14)	+7.87450E-05	1.94570E-05	0.00490	
	Tb(t-1)Tb(t-15)	-2.23990E-03	6.05010E-06	0.00713	
Tc(t)		+1.25200E+02	5.92730E-06	0.31972	
	Tb(t-6)Tb(t-15)	+1.74160E-03	5.07420E-06	0.00656	
	Tb(t-2)Tb(t-15)	+1.78220E-03	3.47450E-06	0.00867	
	Tb(t-4)Tb(t-15)	-1.39840E-03	3.18420E-06	0.00762	
	Tc(t-2)Tc(t-2)	+7.99860E-01	3.14330E-06	0.62961	
	Tc(t-1)Tc(t-2)	-1.43800E+00	2.58890E-06	0.41378	
	Tb(t-13)Tb(t-15)	+1.00040E-03	2.42010E-06	0.00833	
	Tb(t-12)Tb(t-15)	-7.09400E-04	2.06130E-06	0.00789	

Table 2. NARX models for diagnosing PHP dynamics at 80 W

model		andfiniant EDD		Standard
model	terms	coefficient	ERR	deviation
	Tb(t-1)	+9.87190E-01	9.99670E-01	0.10525
	Ta(t-13)	+4.91430E-02	3.79920E-05	0.02717
	Tb(t-2)	-2.53470E-01	1.28860E-05	0.13946
	Tb(t-5)	+1.84240E-01	8.96160E-06	0.10266
	Ta(t-4)Ta(t-4)	+3.05000E-02	8.66170E-06	0.01060
	Ta(t-7)Ta(t-8)	+1.77270E-04	4.70450E-06	0.00067
	Ta(t-15)	+5.98320E-02	4.57480E-06	0.02971
Tb(t)	Ta(t-5)Ta(t-5)	+1.81390E-02	4.27010E-06	0.00916
	Tb(t-4)	-1.94230E-01	3.91960E-06	0.12970
	Ta(t-2)Ta(t-2)	-1.38240E-02	3.41940E-06	0.00396
	Tb(t-3)	+1.64300E-01	1.82470E-06	0.10199
	Ta(t-4)Ta(t-5)	-6.20610E-02	1.72180E-06	0.02124
	Ta(t-1)Ta(t-4)	+1.42320E-03	1.26080E-06	0.00095
	Ta(t-2)Ta(t-5)	+2.62970E-02	7.43550E-07	0.00805
	Ta(t-6)Ta(t-8)	-8.55510E-04	6.60580E-07	0.00087
	Tc(t-1)	+9.68650E-01	9.99870E-01	0.02215
	Tb(t-4)	-1.36820E-01	1.01070E-05	0.15060
	Tc(t-5)Tb(t-2)	-1.86820E-02	5.16370E-06	0.02012
	Tb(t-5)	+1.12690E-01	3.38020E-06	0.09149
	Tc(t-4)Tb(t-4)Tb(t-8)	-1.17620E-03	2.98840E-06	0.00039
	Tc(t-2)Tb(t-1)Tb(t-4)	+5.55450E-05	2.65820E-06	0.00003
	Tc(t-4)Tb(t-1)Tb(t-5)	+8.21120E-04	2.34630E-06	0.00048
Tc(t)	Tb(t-3)	+1.08320E-02	1.39730E-06	0.08328
	Tc(t-5)Tb(t-4)Tb(t-8)	+1.23990E-03	1.24310E-06	0.00039
	Tc(t-5)Tb(t-1)Tb(t-5)	-9.04840E-04	1.23390E-06	0.00049
	Tc(t-3)Tb(t-1)Tb(t-6)	-3.78680E-07	9.47540E-07	0.00002
	Tc(t-4)Tb(t-2)	+2.04910E-02	8.64180E-07	0.01993
	Tc(t-3)Tb(t-7)Tb(t-8)	-1.61560E-05	7.64660E-07	0.00001
	Tc(t-2)Tb(t-3)Tb(t-8)	-4.28750E-05	6.44450E-07	0.00003
	Tb(t-6)Tb(t-8)	+4.22300E-04	4.37020E-07	0.00043

Table 3. NARX models for diagnosing PHP dynamics at 120 W.

model	terms	coefficient	ERR	Standard deviation
	Tb(t-1)	+4.80680E-01	9.99280E-01	0.27148
	Ta(t-1)Ta(t-1)	+7.34480E-04	3.54670E-05	0.00044
	Tb(t-2)	+1.15520E+00	2.29450E-05	0.55217
	Tb(t-1)Tb(t-3)	+8.54460E-03	1.49640E-05	0.00366
	Tb(t-3)	-8.20980E-01	1.33750E-05	0.36506
	Ta(t-9)	-1.66460E-01	1.27850E-05	0.07869
	Ta(t-15)	+2.69530E-01	1.18730E-05	0.13212
Tb(t)	Ta(t-3)Ta(t-4)	-2.43310E-03	1.15690E-05	0.00088
	Tb(t-2)Tb(t-2)	-1.04270E-02	8.39190E-06	0.00372
	Ta(t-2)Ta(t-5)	+2.48160E-03	5.69370E-06	0.00113
	Ta(t-3)Ta(t-15)	-2.07410E-03	5.12350E-06	0.00149
	Ta(t-2)Ta(t-6)	-1.06210E-03	2.83330E-06	0.00099
	Ta(t-10)	+9.11610E-02	2.59290E-06	0.07987
	Ta(t-13)	-5.10410E-02	2.01980E-06	0.06224
	Tb(t-3)Ta(t-3)	+4.63400E-03	1.60700E-06	0.00292
	Tc(t-1)	+9.20850E-01	9.99600E-01	0.06234
	Tc(t-1)Tc(t-1)Tb(t-8)	+4.73310E-06	1.87000E-05	0.00005
	Tc(t-2)Tc(t-2)Tc(t-2)	-2.36940E-05	1.16210E-05	0.00005
Tc(t)	Tc(t-2)Tc(t-2)Tb(t-9)	+5.36190E-05	7.40940E-06	0.00007
	Tb(t-10)	-4.52450E-01	6.82750E-06	0.12830
	Tb(t-3)Tb(t-9)Tb(t-9)	+4.23060E-05	5.27120E-06	0.00003
	Tb(t-9)	+4.58490E-01	4.88810E-06	0.12956
	Tb(t-2)Tb(t-6)	-1.39190E-03	4.56690E-06	0.00217
	Tb(t-1)Tb(t-4)Tb(t-8)	-1.04140E-04	4.09540E-06	0.00006

Tb(t-2)Tb(t-4)Tb(t-6)	-6.03920E-05	3.97280E-06	0.00003
Tc(t-	1)Tb(t-8)	+5.68870E-03	3.69750E-06	0.00193
Tb(t-3)Tb(t-10)Tb(t-10)	+9.97650E-05	3.65970E-06	0.00004
Tc(t-1)	Tc(t-1)Tc(t-1)	-9.65940E-05	3.07020E-06	0.00005
Tb(t-	-3)Tb(t-7)	-5.19430E-03	2.78620E-06	0.00139
Tb(t-	-1)	+2.99970E-02	1.77600E-06	0.05552

V. CONCLUSIONS

The presented PHP with hollow cylindrical configuration developed was high-performance thermal management. The experiment validated that flow circulation throughout the start-up procedure multiperiodic oscillations not only functioned as the key factor activating the PHP but also influenced characterized and the **PHP** performance.

This executed study proposes new means through which PHP dynamics can be diagnosed via NARX modeling. The ANN-based realistic modeling means produced reasonable results accomplished via massive training data and several algorithms. All the models in this study were determined to be efficacious because more than 97% of simulated results were within a relative error less than ±30%. This demonstrates that the proposed modeling means is useful to locate and diagnose the thermal instability of PHPs. Moreover, the merit of this modeling means in providing diagnostic information can be utilized in controller design for the PHP start-up procedures.

The employed GFRFs provided a method of feature visualization to capture and explain nonlinear frequency-domain phenomena in various PHP dynamic states. Accordingly, the PHP dynamics could be characterized as being complicated patterns of resonances on multidimensional energy spectra. This resonance analysis based on the theory of Volterra series can be used as a recognition technique to diagnose the intrinsic features of PHPs.

ACKNOWLEDGEMENTS

The authors appreciate the Ministry of Science and Technology, Republic of China, Taiwan, for funding this research work under Contract MOST 106-2218-E-606 -007 -MY2.

REFERENCES

- [1] R.J. McGlen, R. Jachuck, and S. Lin, "Integrated thermal management techniques for high power electronic devices", Appl. Therm. Eng. 24 (2004) 1143–1156.
- [2] R. Kandasamy, X.Q. Wang, and A.S. "Mujumdar, Application of phase change materials in thermal management of electronics", Appl. Therm. Eng. 27 (2007) 2822–2832
- [3] S.M.S. Murshed, and C.A.Nieto de Castro, "A critical review of traditional and emerging techniques and fluids for electronics cooling", Renew. Sust. Energ. Rev. 78 (2017) 821–833.
- [4] H. Akachi, "Structure of a heat pipe", US Patent 4,921,041, 1990.
- [5] A. Faghri, "Review and advances in heat pipe science and technology", J. Heat Transfer 134 (2012), 123001.
- [6] X. Han, X. Wang, H. Zheng, X. Xu, and G. Chen, "Review of the development of pulsating heat pipe for heat dissipation", Renew. Sust. Energ. Rev. 59 (2016) 692–709.
- [7] S. Khandekar, P. Charoensawan, M. Groll, and P. Terdtoon, "Closed loop pulsating heat pipes Part B: visualization and semi-empirical modeling", Appl. Therm. Eng. 23 (2003) 2021–2033.
- [8] J.L. Xu, Y.X. Li, and T.N. Wong, "High speed flow visualization of a closed loop pulsating heat pipe", Int. J. Heat Mass Tran. 48 (2005) 3338–3351.
- [9] Z.H Xue, and Wei Qu, "Experimental and theoretical research on a ammonia pulsating heat pipe: New full visualization of flow pattern and operating mechanism study", Int. J. Heat Mass Tran. 106 (2017) 149–166
- [10] S. Thongdaeng, B. Bubphachot, and S. Rittidech, "Two-phase flow patterns of a top heat mode closed loop oscillating heat pipe with check valves (THMCLOHP/CV)", J Appl Mech Tech Ph+. 57 (2016) 1101–1107.
- [11] P. Sakulchangsatjatai, P. Terdtoon, T. Wongratanaphisan, P. Kamonpet, and M. Murakami, "Operation modeling of closed-end and closed-loop oscillating heat

- pipes at normal operating condition", Appl. Therm. Eng. 24 (2004) 995–1008.
- [12] X.S.Yang, M. Karamanoglu, T. Luan, and S. Koziel, "Mathematical modelling and parameter optimization of pulsating heat pipes", J. Comput. Sci. 5 (2014) 119–125.
- [13] M. Ebrahimi Dehshali, M.A. Nazari, and M.B. Shafii, "Thermal performance of rotating closed-loop pulsating heat pipes: Experimental investigation and semi-empirical correlation", Int. J. Therm. Sci. 123 (2018) 14–26.
- [14] A. Jokar, A.A. Godarzi, M. Saber, and M. B. Shafii, "Simulation and optimization of a pulsating heat pipe using artificial neural network and genetic algorithm", Heat Mass Transf. 52 (2016) 2437–2445.
- [15] M. H. Ahmadi, A. Tatar, M.A. Nazari, R. Ghasempour, A.J. Chamkha, and W.M. Yan, "Applicability of connectionist methods to predict thermal resistance of pulsating heat pipes with ethanol by using neural networks", Int. J. Heat Mass Tran. 126, Part B (2018) 1079–1086.
- [16] J. L. Xu, and X. M. Zhang, "Start-up and steady thermal oscillation of a pulsating heat pipe", Heat Mass Transf. 41 (2005) 685–694.
- [17] W. Qu, and H.B. Ma, "Theoretical analysis of startup of a pulsating heat pipe", Int. J. Heat Mass Tran. 50 (2007) 2309–2316.
- [18] I. Nekrashevych, and V.S. Nikolayev, "Effect of tube heat conduction on the pulsating heat pipe start-up", Appl. Therm. Eng. 117 (2017) 24–29.
- [19] C.Y. Tseng, K.S. Yang, K.H. Chien, S.K. Wu, and C. C. Wang, "A novel double pipe pulsating heat pipe design to tackle inverted heat source arrangement", Appl. Therm. Eng. 106 (2016) 697–701.
- [20] R.J. Xu, X.H. Zhang, R.X. Wang, S.H. Xu, and H.S. Wang, "Experimental investigation of a solar collector integrated with a pulsating heat pipe and a compound parabolic concentrator", Energy Convers. Manag. 148, (2017) 68–77.
- [21] X. Liu, Y. Chen, and M. Shi, "Dynamic performance analysis on start-up of closed-loop pulsating heat pipes (CLPHPs)", Int. J. Therm. Sci. 65 (2013) 224–233.
- [22] F. Ding, "Hierarchical multi-innovation

- stochastic gradient algorithm for Hammerstein nonlinear system modeling", Appl. Math. Model. 37 (2013) 1694–1704.
- [23] U. Baur, P. Benner, and L. Feng, "Model order reduction for linear and nonlinear systems: a system-theoretic perspective", Arch. Comput. Methods Eng. 21 (2014) 331–358.
- [24] S. Mobayen, and D. Baleanu, "Linear matrix inequalities design approach for robust stabilization of uncertain nonlinear systems with perturbation based on optimally-tuned global sliding mode control", J. Vib. Control. 23 (2015) 1285–1295.
- [25] A.A. Khan, and N.S. Vyas, "Non-linear parameter estimation using Volterra and Wiener theories", J. Sound Vib. 221 (1999) 805–821.
- [26] H.T. Jeong, I.S. Chang, and C.D. Kim, "Compensation method for a nonlinear amplifier using the gain expansion phenomenon in a Doherty amplifier", IEEE Trans. Microw. Theory Tech. 54 (2006) 1425 1430.
- [27] P.O. Polack, J. Friedman, and P. Golshani, "Cellular mechanisms of brain state-dependent gain modulation in visual cortex", Nat. Neurosci. 16 (2013) 1331–1339.
- [28] L. Bottou, "From machine learning to machine reasoning", Mach. Learn. 94 (2014) 133–149.
- [29] C. Voyant, G. Notton, S. Kalogirou, M.L. Nivet, C. Paoli, F. Motte, and A. Fouilloy, "Machine learning methods for solar radiation forecasting: A review, Renew". Energ. 105 (2017) 569–582.
- [30] L. Piroddi, and W. Spinelli, "An identification algorithm for polynomial NARX models based on simulation error minimization", Int. J. Control 76 (2003) 1767–1781.
- [31] J.M.P. Menezes Jr., and G.A. Barreto, "Long-term time series prediction with the NARX network: an empirical evaluation", Neurocomputing 71 (2008) 16–18 3335–3343.
- [32] M. Ardalani-Farsa, and S. Zolfaghari, "Chaotic time series prediction with residual analysis method using hybrid Elman–NARX neural networks",

- Neurocomputing 73 (2010) 2540-2553.
- [33] M.D. Buhmann, "Radial basis functions", Acta Numer. 9 (2000) 1–38.
- [34] B. Fornberg, and N. Flyer, "Solving PDEs with radial basis functions", Acta Numerica, 24 (2015) 215–258.
- [35] G.B.Wright, and B. Fornberg, "Stable computations with flat radial basis functions using vector-valued rational approximations", J. Comput. Phys. 331 (2017) 137–156.
- [36] B. Fornberg, E. Lehto, and C. Powell, "Stable calculation of Gaussian-based RBF-FD stencils", Comput. Math. Appl. 65 (2013) 627–637.
- [37] A. Bakhta, E. Cancès, P. Cazeaux, S. Fang, and E. Kaxiras, "Compression of Wannier functions into Gaussian-type orbitals", Comput. Phys. Commun. 230 (2018) 27-37.
- [38] K.M. Ali, and M.J. Pazzani, "Error reduction through learning multiple descriptions", Mach. Learn. 24 (1996) 173–202.
- [39] Y. Zhao, S.A. Billings, H. Wei, and P.G. Sarrigiannis, "Tracking time-varying causality and directionality of information flow using an error reduction ratio test with applications to electroencephalography data", Phys. Rev. E 86 (2012) 051919.
- [40] K. Yamaoka, T. Nakagawa, and T. Uno, "Application of Akaike's information criterion (AIC) in the evaluation of linear pharmacokinetic equations", J. Pharmacokinet. Biopharm. 6 (1978) 165–175.
- [41] O.M. Akpa, and E.I. Unuabonah, "Small-sample corrected Akaike information criterion: an appropriate statistical tool for ranking of adsorption isotherm models", Desalination 272 (2011) 20–26.
- [42] W.K. Liu, and Y. Chen, "Wavelet and multiple scale reproducing kernel methods", Int. J. Numer. Methods Fluids 21 (1995) 901–931.
- [43] D. Xiu, and G.E. Karniadakis, "Modeling uncertainty in flow simulations via generalized polynomial chaos", J. Comput. Phys. 187 (2003) 137–167.
- [44] Y. Wu, and S. Verdu, "Functional Properties of Minimum Mean-Square Error

- and Mutual Information", IEEE Trans. Inform. Theory 58 (2011) 1289–1301.
- [45] A.L. Schubert, D. Hagemann, A. Voss, and K. Bergmann, "Evaluating the model fit of diffusion models with the root mean square error of approximation", J. Math. Psychol. 77 (2017) 29-45.
- [46] W. Wiedermann, and M. Hagmann, "Asymmetric properties of the Pearson correlation coefficient: Correlation as the negative association between linear regression residuals", Commun. Stat. Theory Methods 45 (2016) 6263-6283.
- [47] R. Bujack, H. De Bie, N. De Schepper, and G. Scheuermann, "Convolution products for hypercomplex Fourier transforms", J. Math. Imaging Vis. 48 (2014) 606–624.
- [48] C.M. Cheng, Z.K. Peng, W.M. Zhang, and G. Meng, "Volterra-series-based nonlinear system modeling and its engineering applications: A state-of-the-art review", Mech. Syst. Signal Process. 87 Part A (2017) 340–364.
- [49] X. Yu, "Controlling Lorenz chaos", Int. J. Syst. Sci. 27 (1996) 355–359.
- [50] S.K. Yang, C.L. Chen, and H.T. Yau, "Control of chaos in Lorenz system", Chaos Soliton. Fract. 13 (2002) 767–780.